Journal of Drug Delivery Science and Technology 57 (2020) 101752

Contents lists available at ScienceDirect

Journal of Drug Delivery Science and Technology

journal homepage: www.elsevier.com/locate/jddst

Curcumin-encased hydroxyapatite nanoparticles as novel biomaterials for antimicrobial, antioxidant and anticancer applications: A perspective of nano-based drug delivery

Saleth Sebastiammal[a,b], Arul Sigamani Lesly Fathima[a,*], Sandhanasamy Devanesan[c,d], Mohamad S. AlSalhi[c,d,***], Johnson Henry[e], Marimuthu Govindarajan[f,g], Baskaralingam Vaseeharan[h,**]

[a] Department of Physics, Holy Cross College (Autonomous), Nagercoil, 629004, Tamil Nadu, India
[b] Reg.No:17213042132003, Manonmaniam Sundaranar University, Abishekapatti, Tirunelveli, 627012, Tamil Nadu, India
[c] Research Chair in Laser Diagnosis of Cancers, Department of Physics and Astronomy, College of Science, King Saud University, P.O. Box -2455, Riyadh, 11451, Saudi Arabia
[d] Department of Physics and Astronomy, College of Science, King Saud University, P.O. Box -2455, Riyadh, 11451, Saudi Arabia
[e] Department of Physics, Manonmaniam Sundaranar University, Abishekapatti, Tirunelveli, 627012, Tamil Nadu, India
[f] Unit of Vector Control, Phytochemistry and Nanotechnology, Department of Zoology, Annamalai University, Annamalainagar, 608 002, Tamil Nadu, India
[g] Unit of Natural Products and Nanotechnology, Department of Zoology, Government College for Women (Autonomous), Kumbakonam, 612 001, Tamil Nadu, India
[h] Nanobiosciences and Nanopharmacology Division, Department of Animal Health and Management, Alagappa University, Science Campus, Karaikudi, 630 004, Tamil Nadu, India

ARTICLE INFO

Keywords:
Nanotechnology
Curcumin
Hydroxyapatite
Anticancer
Biological applications

ABSTRACT

Hydroxyapatite (HAp) is an important biological molecule and principal mineral component found in bones that is used in various clinical applications to significantly enhance the biological activity and biocompatibility of man-made biological molecule. Several analyses have been performed to control the structural properties of HAp by varying the processing parameters. This study described the synthesis of HAp nanoparticles (NPs) via the sol-gel method, that would be effective for biomedical applications, such as bone graft substitution. It also examined the effects of pure HAp, surfactant (PEG and CTAB)-assisted HAp NPs, and curcumin-mediated HAp NPs. The synthesized HAp NPs were analyzed using XRD, FTIR, RAMAN, FESEM, TEM, EDAX, UV-DRS, and PL analysis. From the XRD analysis, it was found that the prepared HAp NPs have a hexagonal structure with nanosize distribution. From FESEM and TEM analyses, it was found that the synthesized HAp NPs were rod-like in shape and the elemental analysis was conducted using EDAX. In addition, the biological applications were investigated, viz., antibacterial, antifungal, antioxidant, and anticancer activity. The synthesized HAp nanoparticles possessed excellent antibacterial, antifungal, antioxidant, and anticancer activities. Overall, curcumin-encased HAp nanoparticles can play a vital role in a wide range of fields, including water treatment, food preservation, wound dressing, nanomedicines, and cosmetics as biocidal and disinfecting agents.

1. Introduction

Hydroxyapatite (HAp) nanoparticles (NPs) have received considerable attention over the last decade due to their significant biological applications [1–5]. HAp plays a vital role in biomaterial engineering due to its enhanced biocompatibility and bioactivity [6–9]. The stoichiometric ratio of calcium and phosphorous in HAp is 1.67, which resembles that of human bones, and calcium phosphate (CaP) is the major mineral constituent of vertebrae bones and teeth [10–12].

HAp [$Ca_{10}(PO_4)_6(OH)_2$] is a CaP-based biomaterial primarily used in dental and orthopedic applications because of its structural and chemical similarity to bones, teeth, and enamel [13–15]. HAp acts as an

* Corresponding author.
** Corresponding author.
*** Corresponding author. Research Chair in Laser Diagnosis of Cancers, Department of Physics and Astronomy, College of Science, King Saud University, P.O. Box -2455, Riyadh, 11451, Saudi Arabia.
E-mail addresses: leslysat@gmail.com (A.S. Lesly Fathima), malsalhi@ksu.edu.sa (M.S. AlSalhi), vaseeharanb@gmail.com (B. Vaseeharan).

https://doi.org/10.1016/j.jddst.2020.101752
Received 26 March 2020; Received in revised form 10 April 2020; Accepted 12 April 2020
Available online 18 April 2020
1773-2247/

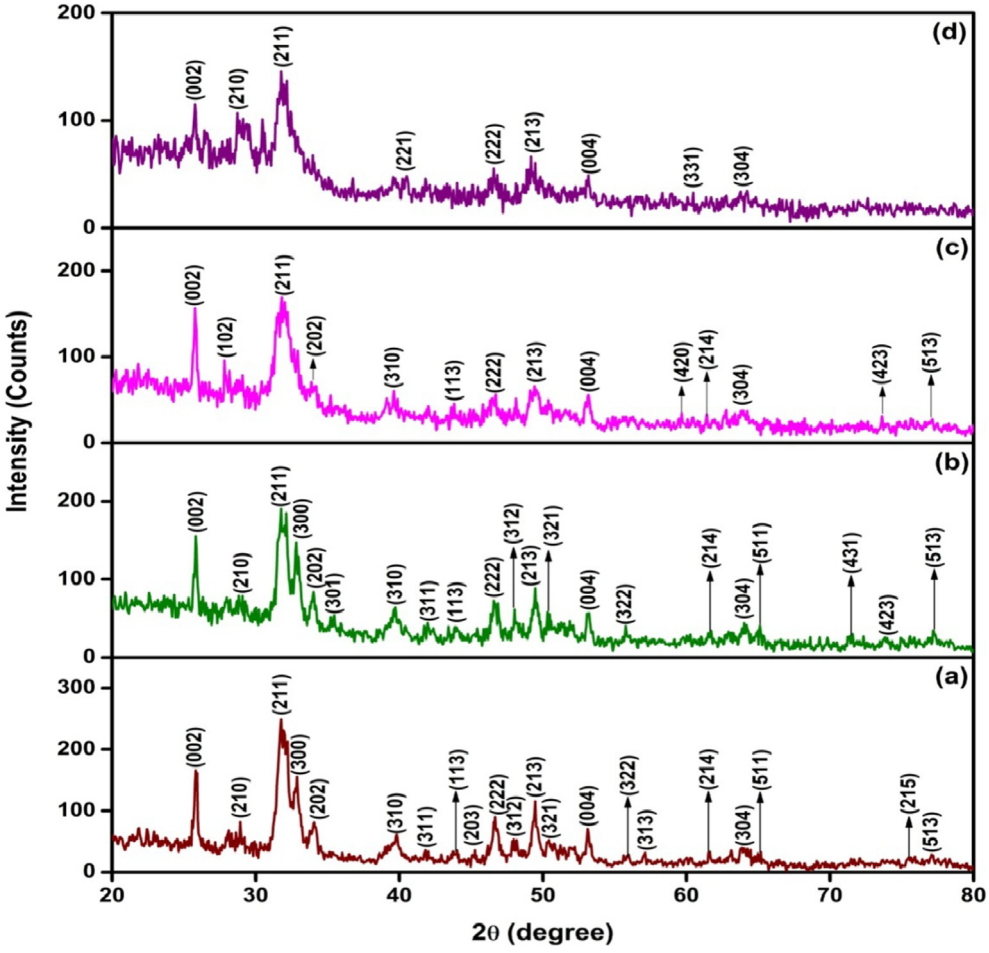

Fig. 1. XRD analysis of HAp NPs calcined at 500 °C. (a) HAp-Pure, (b) HAp-PEG, (c) HAp-CTAB, and (d) HAp-CE.

Table 1
Calculated values for HAp nanoparticles.

Samples	Crystallite Size (nm)	Dislocation density (δ) x 10^{15} (lines/m^2)	Strain (ε) x 10^{-3}	Lattice cell Parameters (Å)		Unit Cell Volume (Å)^3
				a	c	
HAp-Pure	39.07	0.8233	0.0552	9.441	6.877	530.944
HAp-PEG	32.56	1.0386	0.0632	9.417	6.876	528.139
HAp-CTAB	24.41	2.8769	0.1003	9.477	6.871	534.518
HAp-CE	25.57	1.6132	0.0792	9.432	6.886	530.581

implantation compound for biomedical application in the form of coatings and composites on metallic alloys due to its various properties, including osteoinduction, osteoconductivity, osteointegrity, and non-toxicity [16–18]. Due to the potentiality of a rigid control of process parameters, a sol-gel approach is a powerful method for the synthesis of nanophase HAp. HAp NPs synthesized via the sol-gel method can enhance stability and contact at the natural/artificial bone interfaces in both *in vitro* and *in vivo* environments. Recent studies have also demonstrated that HAp particles prohibit the growth of many cancer cell types [19,20]. Synthetic HAp may also be applied in column chromatography for the simple and rapid fractionation of nucleic acids and proteins [21,22]. Moreover, HAp offers convenient qualities for water treatment and remediation for heavy metal contaminated soils [23,24]. Among the different HAp structures, nanosized HAp with appropriate stoichiometry, purity, and morphology have stimulated enormous interest in elemental scientific research and various biomedical applications [25].

Nowadays, size reduced metal nanoparticles have potential biological properties, in particular antibacterial, antifungal, anticancer, antibiofilm, these are development of nano-based drug delivery system [26–30]. Natural resources have been established to reveal vast probable in the biological synthesis of valuable and significant chemicals [31–37]. The present study attempted to synthesize surfactant and curcumin extract (CE)-assisted HAp NPs and analyze the structural, optical, and morphological properties.

2. Materials and methods

2.1. Materials

Calcium nitrate [$Ca(NO_3)_2.4H_2O$], di-ammonium hydrogen phosphate [$(NH_4)_2HPO_4$], cetyl trimethyl ammonium bromide (CTAB), polyethylene glycol (PEG 400), curcumin, and ammonia [NH_3] were procured from Merck chemicals (Germany) or Sigma-Aldrich Co. (USA).

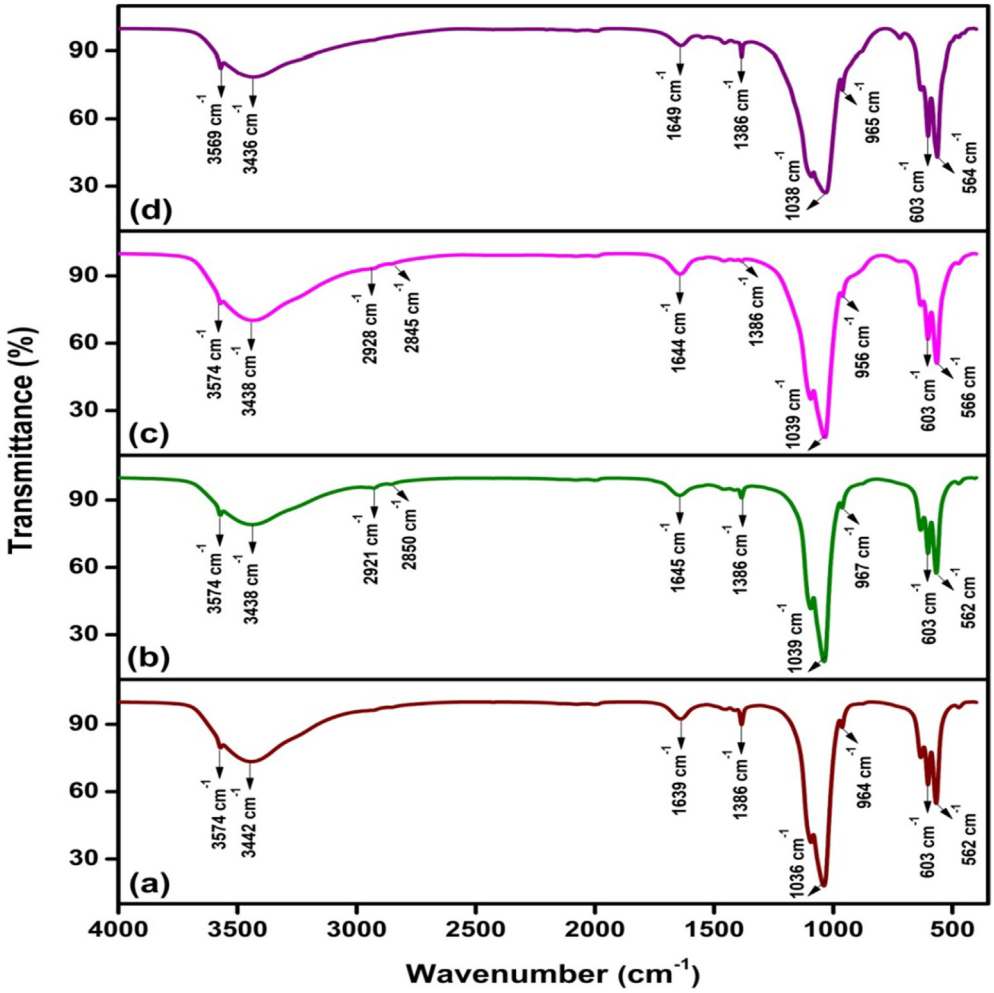

Fig. 2. FTIR spectra of HAp NPs calcined at 500 °C. (a) HAp-Pure, (b) HAp-PEG, (c) HAp-CTAB, and (d) HAp-CE.

Table 2
FTIR band assignments for HAp nanoparticles.

HAp-Pure	HAp-PEG	HAp-CTAB	HAp-CE	Band Assignment
562	562	566	564	Asymmetric bending of PO_4^{3-} (ν_4)
603	603	603	603	Symmetric bending of PO_4^{3-} (ν_4)
964	967	956	965	Symmetric stretching of PO_4^{3-}(ν_1)
1036	1039	1039	1038	Asymmetric stretching of PO_4^{3-} (ν_3)
1386	1386	1386	1386	Carbonate ions (CO_3^{2-}) (ν_3)
1639	1645	1644	1649	Bending mode of H_2O (ν_2)
–	2850	2845	–	(C-H) stretching mode (ν)
–	2921	2928	–	(C-H) stretching mode (ν)
3442	3438	3438	3436	O-H stretching mode
3574	3574	3574	3569	Symmetric stretching of H_2O (ν_1)

All the chemicals used for synthesizing HAp NPs were of analytical reagent grade without any further refinements. Double distilled water was used as a solvent throughout the experiments.

2.2. Synthesis of HAp NPs

HAp powders were synthesized via a sol-gel process using calcium nitrate and di-ammonium hydrogen phosphate with a molar ratio of 1.67 as precursors. First, 1 M of calcium nitrate was dissolved in 50 ml of de-ionized water. Similarly, 0.6 M of di-ammonium hydrogen phosphate solution was prepared and mixed with a calcium nitrate solution under continuous stirring. Then, the aqueous ammonia was added dropwise to the above solution until a pH value of 10 was obtained. The reaction mixture was stirred for 5 h then maintained undisturbed for 24 h at ambient temperature. The obtained precipitate was filtered and washed with distilled water, followed by ethanol and dried at 100 °C for 12 h to obtain white powder. Then, the dried substances were crushed and calcined at 500 °C for 2 h. A similar procedure was adopted for the other three samples with 50 ml of PEG (0.1 M), CTAB (0.1 M), and CE (50 ml).

2.3. Characterizations of HAp NPs

The crystallographic structural analysis was carried out using the X-ray diffraction (XRD) method using an XPERT-PRO powder diffractometer with monochromatic CuKα radiation (λ = 1.5406 Å) over the 2θ range of 20°–80° at a scan rate of 2 m in a Goniometer. The operational voltage and current were 40 kV and 30 mA, respectively. The Fourier-transform infrared (FTIR) spectrum (Bruker IFS 48) was recorded within the range of 4000-400 cm^{-1} using a Micro Raman Spectrometer (LabRAM HR Evolution, HORIBA, France) and was used to identify the functional groups present in HAp. The elemental analysis was conducted using an energy dispersive X-ray spectroscopy (EDX) Bruker detector attached to a field emission scanning electron microscope (FE-SEM) operating at an accelerating voltage of 20 kV. The morphology of HAp NPs was analyzed using a QUANTA 250 FEG (FE-SEM). The microstructures of the synthesized HAp NPs were

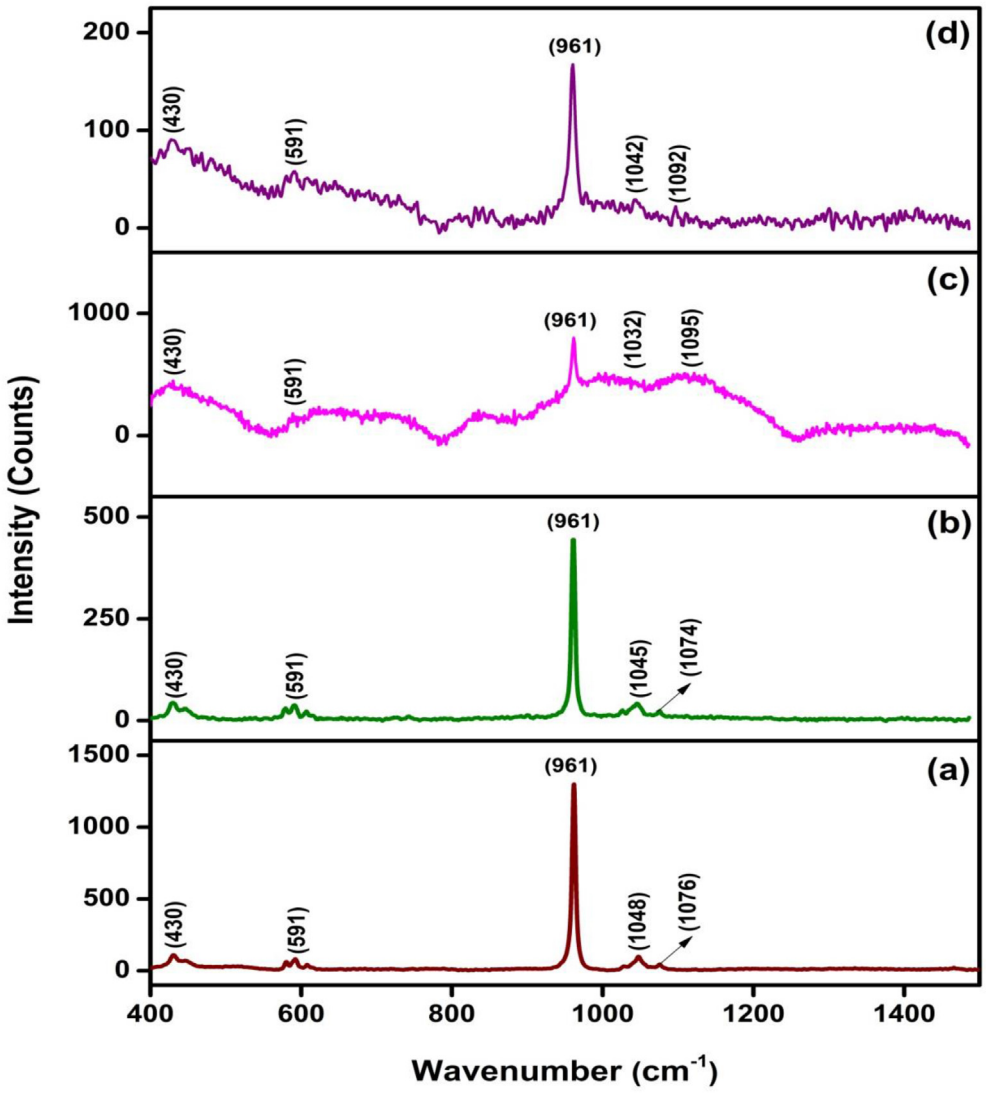

Fig. 3. Raman spectra of HAp NPs calcined at 500 °C. (a) HAp-Pure, (b) HAp-PEG, (c) HAp-CTAB, and (d) HAp-CE.

Table 3
Raman band assignments for HAp nanoparticles.

HAp-Pure	HAp-PEG	HAp-CTAB	HAp-Extract	Band Assignment
430	430	430	430	Symmetric bending mode of PO_4^{3-} (ν_2)
591	591	591	591	Asymmetric bending mode of PO_4^{3-} (ν_4)
961	961	961	961	Symmetric stretching mode of PO_4^{3-} (ν_1)
1048	1045	1032	1042	Asymmetric stretching of PO_4^{3-} (ν_3)
1076	1074	1095	1092	Asymmetric stretching of PO_4^{3-} (ν_3)

investigated using a transmission electron microscope (TEM) JOEL model instrument 1200 EX on carbon-coated copper grids with an accelerating voltage of 80 kV. The optical properties of the samples were studied using a JASCO 650 UV Spectrophotometer. PL studies were carried out using a photoluminescence spectrophotometer (Varian Cary Eclipse) and the emission spectra were recorded at a scan rate of 600 nm/min in the range of 320–600 nm.

2.4. Antibacterial activity of HAp NPs

The antibacterial activity of the synthesized HAp NPs was determined using the well diffusion method. This was performed by sterilizing Mueller Hinton Agar (MHA) media. After solidification, wells were cut on the MHA plates using a cork borer and the test bacterial pathogens were swabbed onto the surfaces of the MHA plates. The samples were placed in the wells and the plates were incubated at 37 °C for 24 h. The zones of inhibition were measured in millimeters. Each antibacterial assay was performed in triplicate and mean values were recorded.

2.5. Antifungal activity of HAp NPs

Antifungal activity of the prepared HAp NPs was determined using the well diffusion method performed by sterilizing PDA (Potato Dextrose Agar) media. After solidification, wells were cut on PDA using a cork borer and the test fungal pathogens were swabbed onto the surface of the PDA plates. The samples were placed into the wells and the plates were incubated at 37 °C for 94 h, and the zones of inhibition

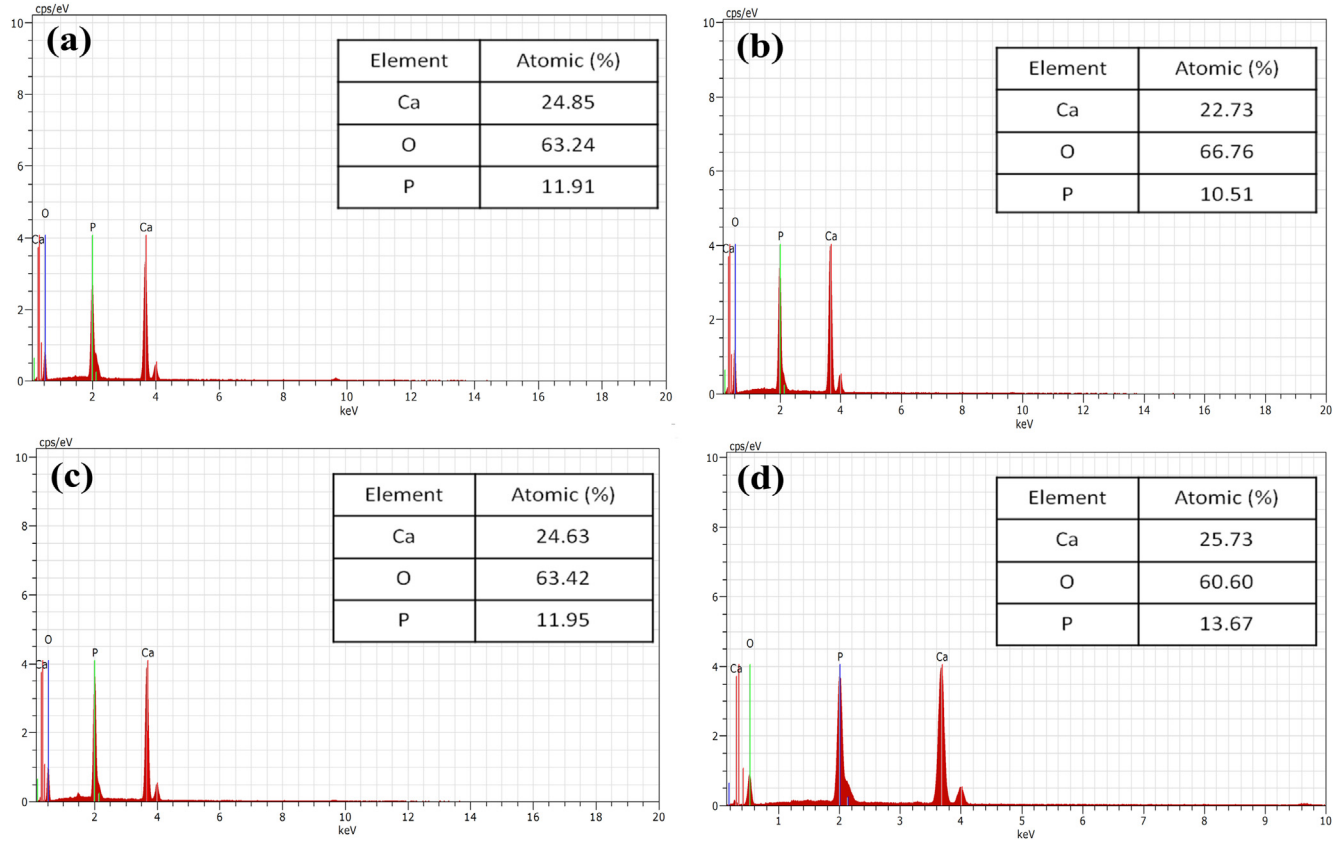

Fig. 4. EDAX spectra of HAp NPs calcined at 500 °C. (a) HAp-Pure, (b) HAp-PEG, (c) HAp-CTAB, and (d) HAp-CE.

Table 4
Elemental compositions for HAp nanoparticles.

Samples	Calcium (Atomic %)	Oxygen (Atomic %)	Phosphate (Atomic %)
HAp-Pure	24.85	63.24	11.91
HAp-PEG	22.73	66.76	10.51
HAp-CTAB	24.63	63.42	11.95
HAp-CE	25.73	60.60	13.97

were measured in millimeters. Each antifungal assay was performed in triplicate and mean values were reported.

2.6. Antioxidant activity of HAp NPs

The DPPH (2,2-diphenyl-2-picrylhydrazyl hydrate) assay was conducted according to the methods of Brand-Williams et al. [38] with some modifications. The scavenging and antioxidant potentials of the samples were evaluated by the ability of the samples to scavenge the stable free radical DPPH. Different concentrations (100-400 µg/ml) of the samples as well as the samples with NPs were separately mixed with 3 ml of 0.1 mM DPPH and incubated in darkness for 15 min. Rutin was used as a standard and the DPPH methanol reagent without the sample was used as the control. The reaction mixture was mixed well and maintained in darkness at 32 °C for 30 min. The degree of decolourization from purple to yellow was measured spectrophotometrically at 517 nm.

The scavenging ability of the samples was calculated using the following equation:

$$\text{DPPH scavenging activity } (\%) = \frac{(\text{Abs control} - \text{Abs sample})}{(\text{Abs control})} \text{X100}$$

2.7. Cytotoxic activity of HAp NPs

The cytotoxic effects of HAp-pure, HAp-PEG, HAp-CTAB, and HAp-curcumin against the HeLa cell line were evaluated using an MTT Assay. HeLa cell lines were initially procured from the National Centre for Cell Sciences (NCCS), Pune, India. The cell line was cultured in 25 cm^2 tissue culture flasks with Dulbecco's modified Eagle's medium (DMEM, Himedia) supplemented with 10% FBS (fetal bovine serum), L-glutamine, sodium bicarbonate, and antibiotic solution containing penicillin (100 U/ml), streptomycin (100 µg/ml), and amphoteracin B (2.5 µg/ml). Cultured cell lines were maintained at 37 °C in a humidified 5% CO_2 incubator (Galaxy® 170 Eppendorf, Germany).

A two-day-old confluent monolayer of cells was trypsinized and the cells were suspended in 10% FBS-supplemented DMEM. The 100 µl cell suspension (5×10^4 cells/well) was then seeded in a 96-well tissue culture plate and incubated at 37 °C in a humidified 5% CO_2 incubator. After 24 h, the growth medium was removed and cells were treated with 5% DMEM with different concentrations (6.25, 12.5, 25, 50, and 100 µg) of 100 µl freshly-prepared samples in triplicate, and incubated at 37 °C in a humidified 5% CO_2 incubator.

The viability of the cells was evaluated by direct observation using an inverted phase contrast microscope followed by MTT assay.

2.8. Statistical analysis

In the present study, all the investigation results were done in three replicates and the outcomes were articulated as mean ± Standard Deviation (SD). Data were subjected to analysis of variance (ANOVA) and Tukey's HSD test ($P = 0.05$). SPSS software version 21.0 was used for the statistical analysis.

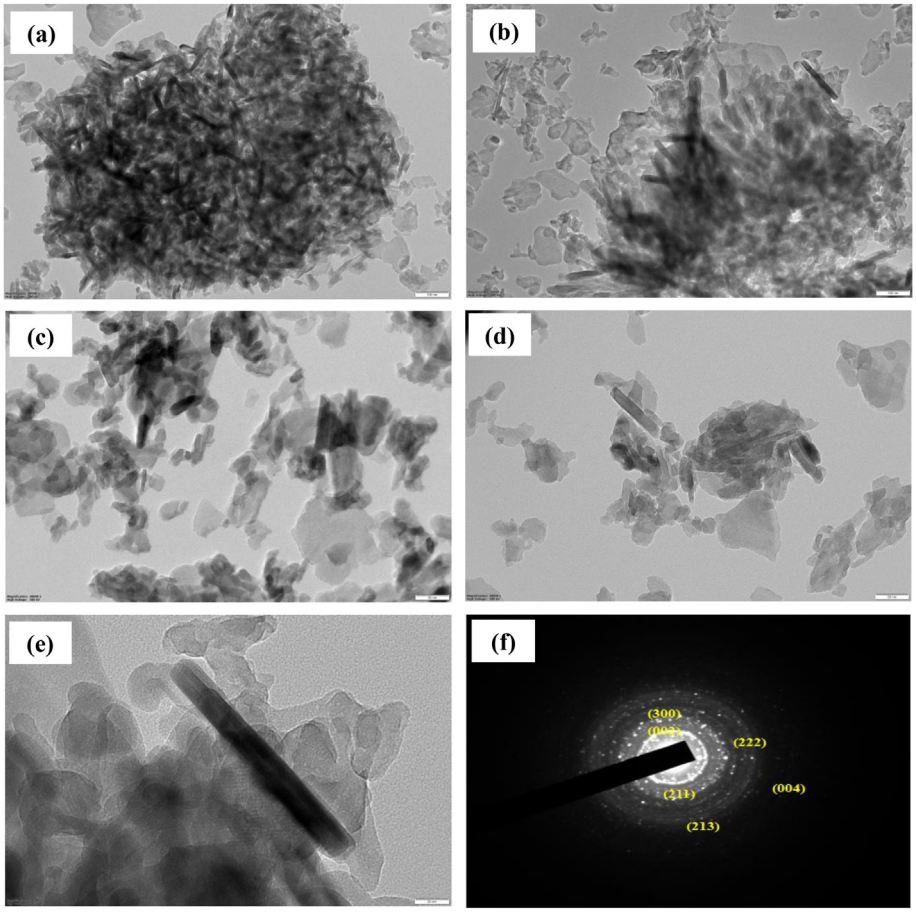

Fig. 5. TEM images for HAp NPs with a magnification of (a) 40000X, (b) 40000X, (c) 80000X, (d) 80000X, (d) 200000X, and (f) SAED pattern.

3. Results and discussion

3.1. XRD analysis

The X-ray diffraction study was used to confirm the crystalline nature of the particles. The XRD patterns of HAp prepared with and without surfactants are provided in Fig. 1. As seen in Fig. 1(a), the HAp prepared without surfactant showed peaks at 2θ = 25.853, 28.529, 31.720, 32.872, 34.204, 39.799, 41.879, 43.891, 46.686, 49.425, 52.028, 53.123, 55.779, and 64.042 due to the diffraction of (002), (210), (211), (300), (202), (310), (311), (113), (222), (213), (402), (004), (322), and (304) planes, respectively. The observed planes are in accordance with the expected pattern of HAp possessing the hexagonal structure with the space group $P6_3/m$ (JCPDS No: 09-0432). No other impurity peaks, such as CaPs and calcium hydroxide, were found, which indicates that the synthesized product is a monophase of HAp under these experimental conditions. The results were in agreement with those of previous studies by Azzaoui et al. [39] and Salarian et al. [40].

The XRD pattern of PEG-assisted HAp (Fig. 1(b)) showed peaks at 2θ = 25.853, 28.552, 31.659, 32.080, 32.906, 33.982, 39.635, 42.065, 43.865, 46.721, 48.164, 49.494, 53.143, 55.879, 64.078, and 77.175, which belong to the diffraction of (002), (210), (211), (112), (300), (202), (310), (311), (113), (222), (312), (213), (004), (322), (304), and (513) planes, respectively. The obtained peaks were similar to those of HAp prepared without surfactant. The intensity of the prominent peaks decreased, while the 2θ of the (211) plane shifted slightly toward the lower angle (31.720–31.659) with respect to HAp without surfactant.

Fig. 1(c) depicts the XRD pattern of HAp with CTAB surfactant. The obtained XRD pattern was similar to that of HAp prepared without surfactant; however, the intensity was reduced. The XRD profile of HAp with CTAB shows lower intensity diffraction features than that of HAp fabricated without surfactant. Moreover the intensity of the major peak was shifted toward a higher angle (31.720–32.197) with respect to HAp without surfactant. The surfactant did not affect the crystal system, which indicates the self-compensating ability of HAp [41]. A similar result was previously reported by Kumari et al. [42] for CTAB and SDS surfactant-assisted HAp NPs. Fig. 1(d) represents the XRD pattern of CE-assisted HAp NPs. The same diffraction profile was observed for HAp with CE. However, some peaks were not present due to CE potentially preventing the growth of HAp. It was concluded from the XRD pattern that the addition of surfactants reduced the intensity of the diffraction peaks but the crystalline phase of HAp persisted.

The lattice parameter values were calculated through unit cell software, which is listed in Table 1. The obtained lattice constants and cell volumes of the prepared HAp NPs are in strong agreement with the standard data a = 9.418 Å, c = 6.884 Å and V = 528.80 $Å^3$ (JCPDS Card No.: 09-0432). The average crystallite size and microstrain can be estimated from the XRD data as both parameters affect the peak shape.

The prepared HAp was polycrystalline in nature and, hence, a large number of crystallites with various orientations and positions caused variations in the phase difference between the scattered waves. The total intensity scattered by all crystallites is the sum of individual intensities scattered by each crystallite. The diffraction peaks at (0 0 2), (2 1 1), and (3 0 0) planes were taken to calculate the average crystallite size as they were sharper as well as isolated, and the results are presented in Table 1. The crystallite size was found to be approximately 39.07, 32.56, 24.41, and 25.57 nm for the samples prepared without and with surfactant PEG, CTAB, and CE, respectively. The peaks were significantly broadened in HAp with CTAB, indicating poor crystallinity

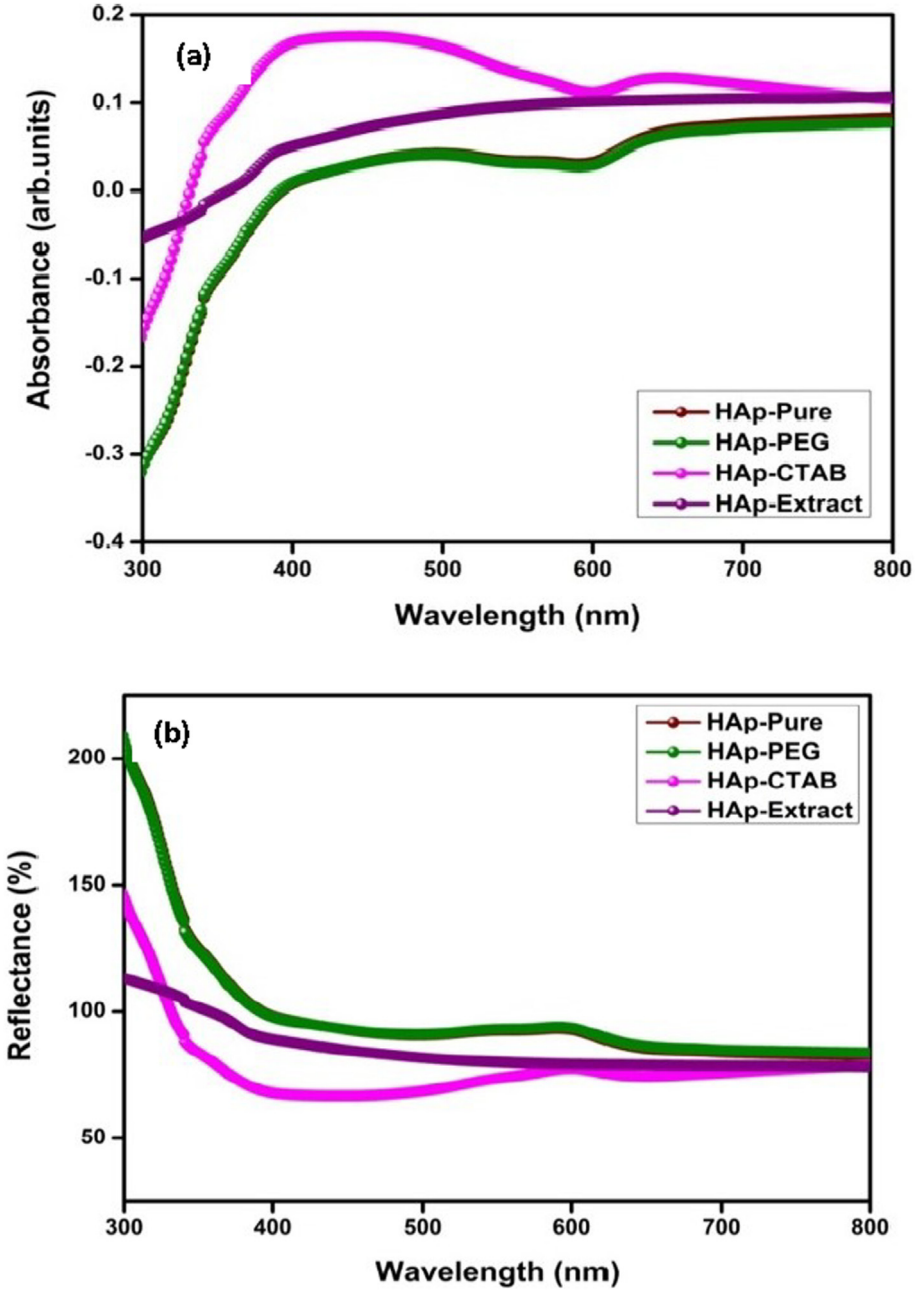

Fig. 6. UV-DRS analysis of absorption (a) and reflection (b) spectra of HAp NPs.

and small crystalline size.

Stress is an important unfavorable factor that affects structural properties, and can result from geometric mismatch at boundaries. These stresses can produce microstrains (ε) in the NPs. The microstrains can be determined from the following relationship:

$$\varepsilon_{str} = \beta/4 \tan\theta$$

The dislocation density was estimated using the following relationship:

$$\delta = 15\varepsilon/aD$$

The calculated microstrain and dislocation density values are presented in Table 1. The microstrain values increased for HAp-CTAB (0.1003) and HAp-extract (0.0792) NPs compared to HAp-pure NPs, indicating a decrease in crystallite size.

3.2. FTIR spectroscopy analysis

The FTIR analysis was undertaken to identify unknown species, functional groups, and vibrational modes associated with each peak. The FTIR spectrum of HAp NPs recorded using the KBr pellet technique is shown in Fig. 2(a–d). The FTIR spectra of HAp NPs prepared with and without surfactant and the vibrational assignments are provided in Table 2. Fig. 2(a) shows the FTIR spectrum of HAp NPs prepared without surfactant, exhibiting the vibrations of the functional groups at various wavenumbers of IR radiation. Initially, the bands observed at 562 and 603 cm^{-1} were due to ν_4 bending vibrations of PO_4^{3-}. A weak peak located at 964 cm^{-1} was assigned to the symmetric stretching mode of PO_4^{3-}. The strong and sharp peak observed at 1036 cm^{-1} was assigned to the asymmetric stretching mode of PO_4^{3-}. The low intensity band at 1386 cm^{-1} corresponded to the CO_3^{2-} functional group, which may be due to the interaction between the HAp precursor solutions with atmospheric CO_2. The peaks at 3442 and 1639 cm^{-1}

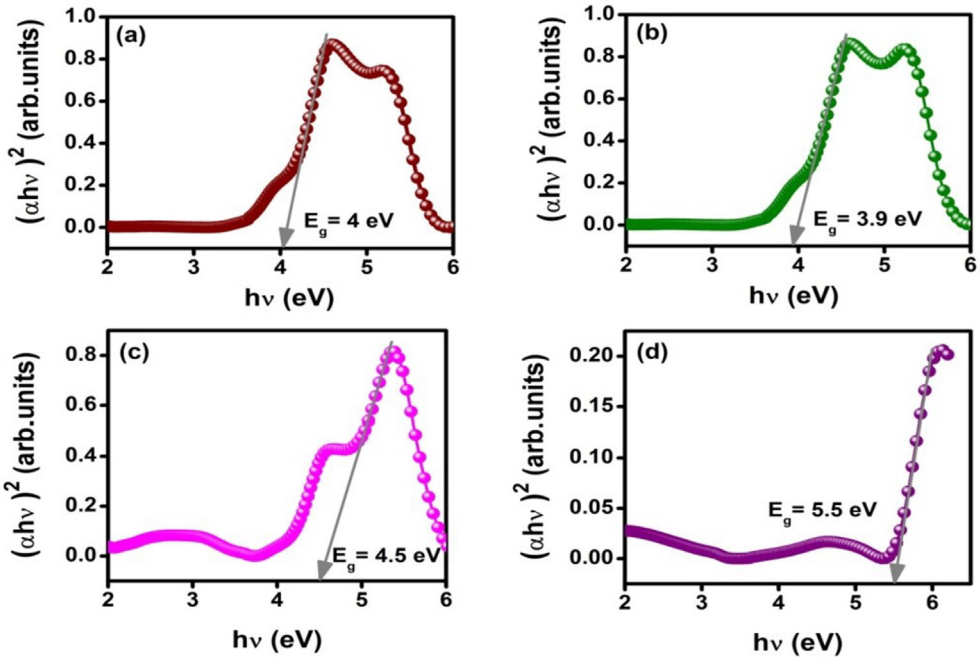

Fig. 7. KM plot for HAp NPs calcined at 500 °C. (a) HAp-Pure, (b) HAp-PEG, (c) HAp-CTAB, and (d) HAp-CE.

were due to the observed water molecules, while the broad peak at 3442 cm^{-1} was due to the stretching mode of OH^-, and the peak at 1639 cm^{-1} was assigned to the bending mode of water. The weak peak observed at 3574 cm^{-1} also corresponds to the OH^- vibrations in the nano HAp lattice. The observed bands from the FTIR spectrum of HAp without surfactant indicated the existence of phosphate and hydroxyl vibrational modes for the formation of HAp. The bands observed in the experiment are in agreement with the reported values of HAp.

Fig. 2(b and c) show FTIR patterns of HAp prepared with surfactants, and their frequency assignments are provided in Table 2. The FTIR spectra of HAp prepared with surfactants PEG and CTAB showed similar profiles to those of pure HAp samples. Some additional low intensity peaks were observed at 2850 and 2921 cm^{-1} for HAp-PEG, and 2845 and 2928 cm^{-1} for HAp-CTAB, which, according to the ν (C-H) stretching vibration bands, were attributed to residual surfactants (PEG/CTAB), showing that the organic surfactant had not been thoroughly washed away and remained in the obtained HAp samples [43,44]. Fig. 2(d) shows the FTIR pattern of HAp prepared with 50 ml CE. The presence of all functional groups in HAp NPs prepared without and with surfactants (PEG and CTAB) was also confirmed in CE-assisted HAp, but a slight decrease in intensity was observed.

From the FTIR spectra, it was concluded that all functional groups of HAp NPs were observed without any additional absorption bands, and the observed band assignments indicate that the synthesized samples were high-quality HAp nanopowders. The FTIR spectra confirm the formation of HAp, and the results were supported by XRD analysis.

3.3. Raman spectroscopy

Raman spectroscopic analysis was used to verify the presence of the pure HAp phase as this method is more sensitive to the existence of secondary phases than X-ray powder diffraction. Raman spectra were recorded in the region 400-1500 cm^{-1} at room temperature for all samples. The Raman spectra of all samples were approximately identical. The HAp NPs prepared without surfactant, with PEG, with CTAB surfactants, and with CE added via sol-gel synthesis are presented in Fig. 3(a–d). The Raman band positions and their frequency assignments are presented in Table 3.

Fig. 3 (a) shows the Raman spectrum of HAp NPs prepared without surfactant. The vibrational bands observed in the Raman spectrum of HAp NPs without surfactant were attributed to the stretching and bending modes of the phosphate group. The most prominent mode at 961 cm^{-1} was assigned to the symmetric stretching mode of PO_4^{3-} (ν_1), which is the characteristic peak of HAp. A low intensity band at 430 cm^{-1} could be assigned to the symmetric bending mode of PO_4^{3-} (ν_2). The other expected band near 590 cm^{-1} was observed at 591 cm^{-1}, which corresponds to the asymmetric bending mode of PO_4^{3-} (ν_2). The two bands observed at 1048 and 1077 cm^{-1} were caused by the asymmetric stretching mode of PO_4^{3-} (ν_3), which appeared with weak intensity in the Raman spectra of HAp [45].

Fig. 3(b) shows the Raman spectrum of HAp prepared with PEG surfactant and shows the similar major peaks of pure HAp. However, in Fig. 3(b) the two bands observed at 1048 and 1076 cm^{-1} in pure HAp lowered to 1045 and 1074 cm^{-1} for HAp-PEG. The Raman spectrum of HAp prepared with CTAB surfactant is depicted in Fig. 3(c). A decrease in the sharpness of the peaks was observed in CTAB-assisted HAp. The characteristic peak of HAp was observed at 961 cm^{-1}, which was obtained in other HAp samples. Fig. 3(d) shows the Raman spectra of HAp prepared with 50 ml CE. The similar major peaks of pure HAp and their frequency assignments are also presented in Table 3. Like HAp-CTAB, a decrease in the sharpness of the peaks can also be observed. The two bands observed at 1048 and 1076 cm^{-1} in pure HAp shifted to 1042 and 1092 cm^{-1}. The structural properties observed in Raman analysis were in strong agreement with the information derived from XRD and FTIR studies, which confirms the synthesis of crystalline HAp.

3.4. Energy dispersive X-ray analysis (EDAX)

EDAX spectra were utilized for the quantitative elemental analysis of HAp NPs. Fig. 4(a–d) depicts the typical EDAX spectra, the elemental composition of HAp is provided as an inset figure, and the compositional ratios are provided in Table 4. The EDAX spectra indicate the presence of Ca, P, and O with a stoichiometric ratio that confirms the formation of HAp NPs. The EDAX spectra illustrate that the samples are consistent with their elemental compounds, and stoichiometry is as expected. They also confirm the presence of calcium (Ca), phosphorus (P), and oxygen (O) signals of HAp NPs. No other signal of a secondary phase or impurity was detected in the EDAX spectra. This implies that

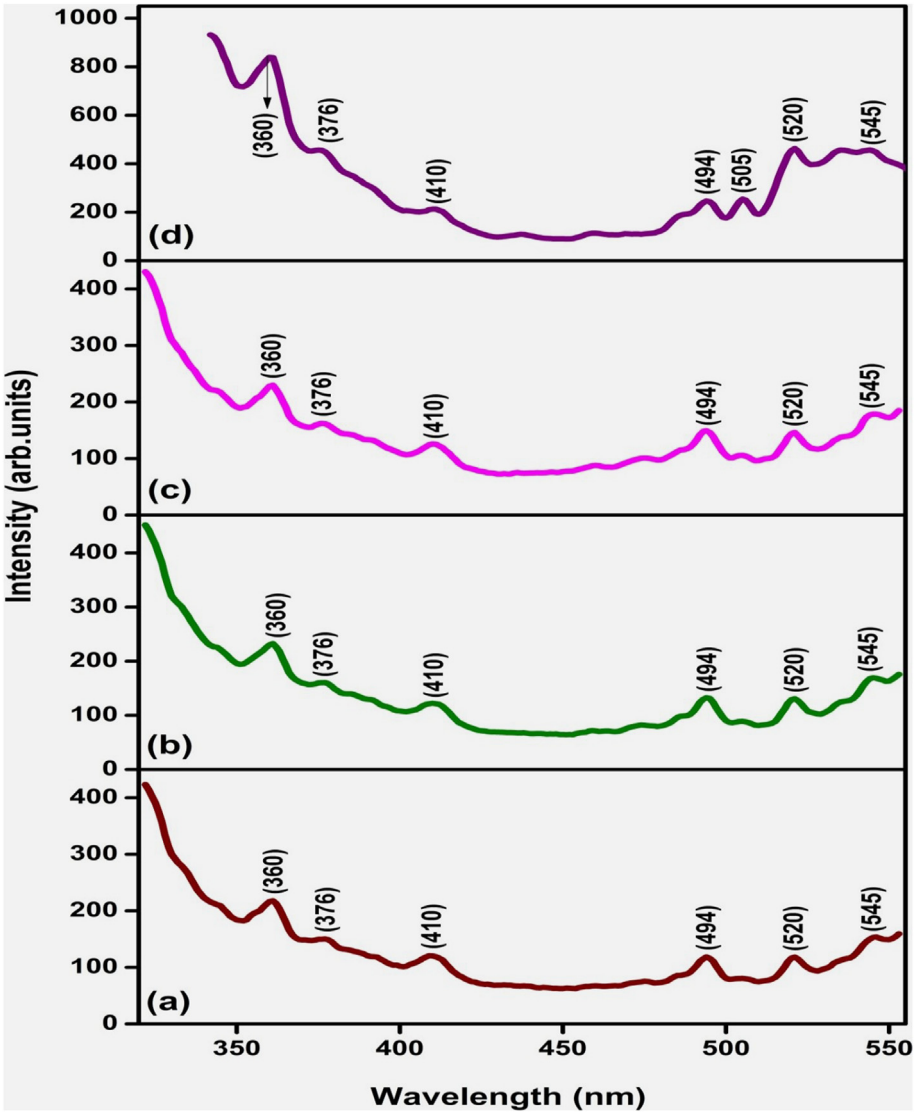

Fig. 8. Photoluminescence spectra for HAp NPs with an excitation wavelength of 320 nm (a) HAp-Pure, (b) HAp-PEG, (c) HAp-CTAB, and (d) HAp-CE.

the prepared HAp NPs are pure in nature. The obtained elemental composition was in strong agreement with the expected values.

Fig. 4 (a) shows the calcium peak at 3.7 keV (Ca kα), revealing that Ca is the main element in HAp. It was observed that the Ca peak was between 0.3 and 0.4 keV (Ca kα), the peak at 2.01 keV (P kα) corresponded to a P peak, and the O peak was observed at 0.5 keV (O kα). The HAp nanopowders have Ca, O, and P in the top portion of the sample with a ratio of 24.85:63.24:11.91%, respectively, for the HAp-pure sample. EDX analysis revealed the main elements of HAp as Ca, O, and P. The quantitative evaluation of all elemental compositions of the powdered sample is shown in Table 4, and was almost equal to the stoichiometric ratio of HAp, proving the stability of the HAp sample. In the present study, H was not present in the EDAX spectra because elements that possesses an atomic number of less than five cannot be detected due to the limitations of the instrument [46].

3.5. FE-SEM analysis

The FE-SEM micrographs revealed the morphology and size distribution of the NPs. The nanometric dimension of the particles was confirmed through an FE-SEM micrograph. Supplementary Figs. 1(a–d) shows the micrographs of HAp prepared with and without surfactant. The FE-SEM images of HAp prepared without surfactant are shown in Supplementary Fig. 1(a). The images show cylindrical- or nanorod-shaped particles, and the lengths of the nanorods were approximately 60–70 nm with an average diameter of approximately 30 nm. The FE-SEM images of PEG, CTAB, and CE assisting HAp shown in Supplementary Figs. 1(b–d) also exhibited rod-like structures with dense and agglomerated particles. From the FE-SEM analysis, it is evident that the surfactant modifies the morphology of HAp.

All FE-SEM micrographs revealed the rod-like morphology of the particles to be highly agglomerated. However, in the CTAB surfactant-assisted sample, HAp nanorods with good dispersibility were observed. All FE-SEM micrographs of HAp NPs exhibited similar agglomeration patterns that consisted of fine crystallites and small sizes, which revealed that the crystal size distribution of bone plays an important role in the remediation of bone fractures [47]. The mean diameters of particles observed in FE-SEM micrographs were below 40 nm for pure HAp, PEG, CTAB, and CE-assisted HAp.

3.6. TEM

A more detailed structural analysis of pure HAp was performed via TEM analysis. The global view of pure HAp NPs without surfactant at different magnifications is depicted in Fig. 5(a–f). TEM analysis provided further insight into the morphology and size of pure HAp. It

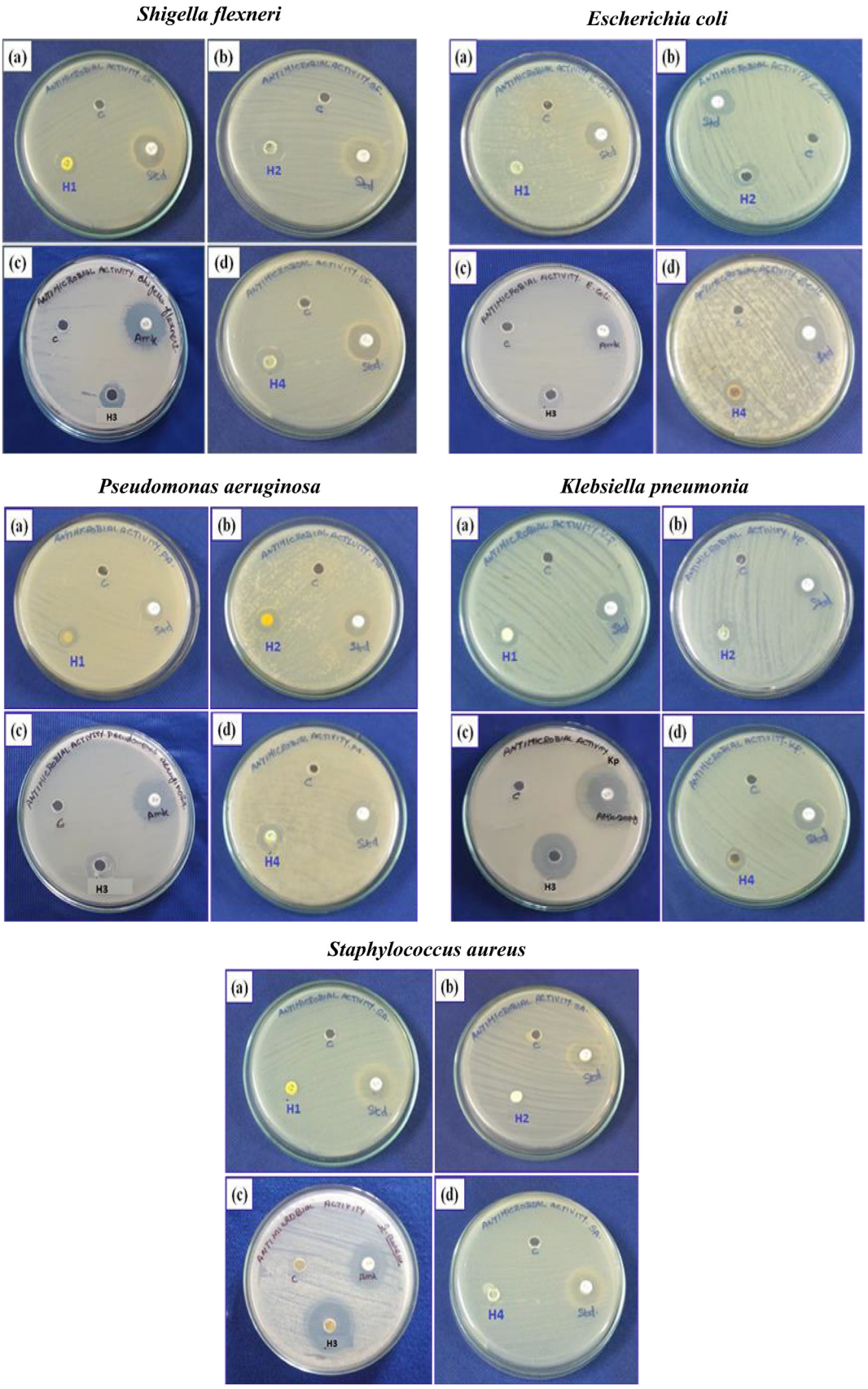

Fig. 9. Antibacterial activity of HAp NPs treated against selected bacteria (a) HAp-Pure, (b) HAp-PEG, (c) HAp-CTAB, and (d) HAp-CE.

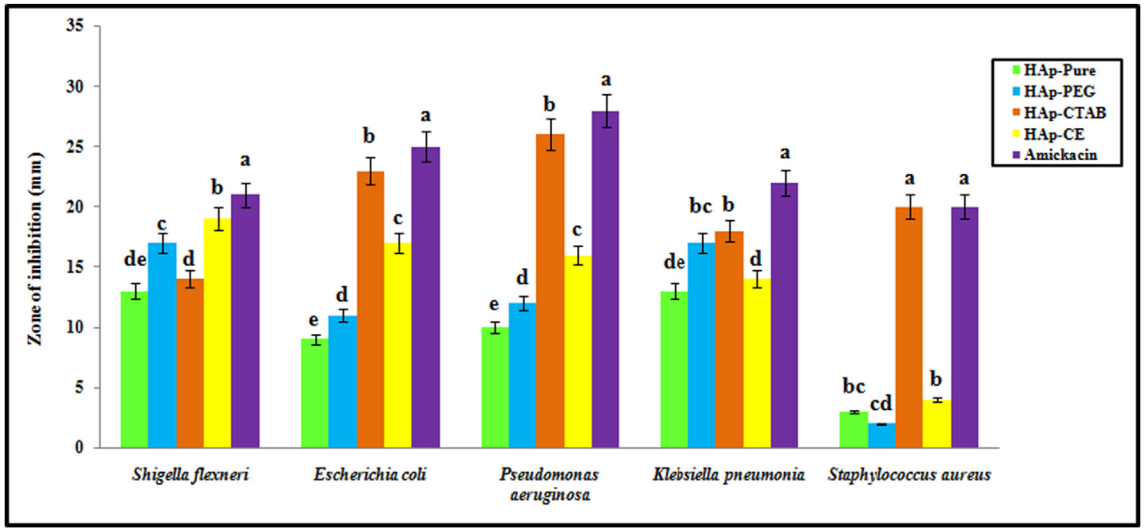

Fig. 10. Antibacterial activity of the HAp NPs treated against bacterial pathogens.

showed a cylindrical rod-like shapes with homogenous microstructures of approximately 40 nm in diameter. Distinct diffraction rings were observed in SAED that correspond to the hexagonal phase of HAp. The intensity of the diffraction rings indicated that the HAp NPs have good crystallinity and a narrow size distribution. The crystalline nature of HAp was evidenced by the SAED pattern with bright circular rings corresponding to the prominent diffraction peaks of hexagonal HAp.

3.7. UV-DRS analysis

The optical properties of HAp NPs were investigated via UV-DRS spectroscopy. The absorbance, reflectance spectra, and band gap energy calculated for the HAp NPs prepared with and without surfactant are provided in Fig. 6. The absorbance spectra of the HAp samples prepared without surfactant and with (PEG/CTAB) surfactants and CE were recorded in the range of 300–800 nm at room temperature. Fig. 6 represents the UV-DRS spectra for HAp NPs showing strong absorption near the low wavelength (UV) region at 350-400 nm, which can be related to the band gap absorption. When compared with pure HAp, CTAB surfactant and CE-assisted HAp show the optical absorption peaks with maximum intensity at around 390 nm, which may be due to absorption in the band gap region.

The optical band gap (Eg) of the HAp NPs was calculated from the KM plot and is shown in Fig. 7. The band gap energy of the samples was measured via the extrapolation of the linear portion of the graph between the modified Kubelka-Munk function $[F(R)\ hv]^2$ versus photon energy (hv). The band values of HAp-pure, HAp-PEG, HAp-CTAB, and HAp-extract were identified as 4, 3.9, 4.5, and 5.5 eV, respectively. The band gap estimated for these samples was slightly lower than the bulk HAp sample (5.5 eV). The band gap of HAp-CTAB and HAp-extract was higher than that of HAp-pure and HAp-PEG, due to the lower crystallite size.

An increase in the optical band gap was observed in HAp-CTAB, and HAp-extract compared to HAp-pure because the surfactant CTAB, and CE could induce the formation of intermediate surface defect states in the band gap region. The increase in the absorption peak intensity and optical band gap values for HAp-CTAB, and HAp-extract compared to HAp-pure were assigned to the reduced crystallite size of the samples. The band gap value obtained in CE-assisted HAp was approximately 5.5 eV, which is in strong agreement with the reported value of HAp with *Moringa oleifera* flower extract. The reported band gap of HAp calculated using density functional theory was approximately 5.23–5.40 eV, and experimental band gap values have been reported from 3.45 to 5.78 eV [48].

3.8. Photoluminescence study

The photoluminescence spectra of synthesized HAp NPs were recorded at room temperature, employing an excitation wavelength of 320 nm for all HAp samples. The HAp samples prepared without surfactant and with PEG, CTAB surfactants, and CE added via sol-gel synthesis and calcined at 500 ˚C are presented in Fig. 8(a–d). The PL emission peaks for HAp ranged from the shorter wavelength of 350 nm to the longer wavelength of 550 nm. The emission peaks at 360, 376, 410, 494, 520, and 545 nm were observed for the samples HAp-pure, HAp-PEG, and HAp-CTAB. Similar emission peaks were present for HAp-extract and one more peak was emitted at 505 nm. The PL emission had four strong and sharp emission bands. A UV emission band at around 360 nm and a blue emission band at around 410 nm were observed. The intense blue emission peaks at around 494 and 520 nm in the visible region were caused by surface defects. The intensity of the emission peak was increased significantly with the addition of CE, which is evident from the bandgap variation obtained in UV-DRS.

3.9. Antibacterial activity of HAp nanorods

The antibacterial activity of the synthesized HAp NPs against five bacterial pathogens was determined via the well diffusion method using sterilized MHA media. The test samples were placed in the wells and the plates were incubated at 37 ˚C for 24 h. The zone of inhibition was measured in millimeters and each antibacterial assay was performed in triplicate, and the mean values were reported.

The novel properties of HAp NPs further encouraged the study of their biological activities. All synthesized compounds were analyzed *in vitro* for their antibacterial activity via the well diffusion assay method. The microbial restriction efficacy of all synthesized HAp samples was evaluated against the human pathogenic bacteria *Shigella flexneri, Escherichia coli*, *Pseudomonas aeruginosa*, *Klebsiella pneumonia*, and *Staphylococcus aureus* based on their toxicity. Among the five most common infection-causing microbes, *E. coli*, *P. aeruginosa*, *K. pneumonia*, and *S. flexneri* are Gram-negative bacteria and *S. aureus* is a Gram-positive bacterium.

The zone of inhibition is the area in which the bacterial growth is blocked due to the bacteriostatic effect of the sample, and it indicates the inhibitory effect of the sample toward a particular microorganism. The zone of inhibition for all bacterial strains was measured and depicted in Figs. 9 and 10. The sizes of the zone of growth inhibition are presented in Supplementary Table 1. All the samples showed maximum activity at a concentration of 50 μg.

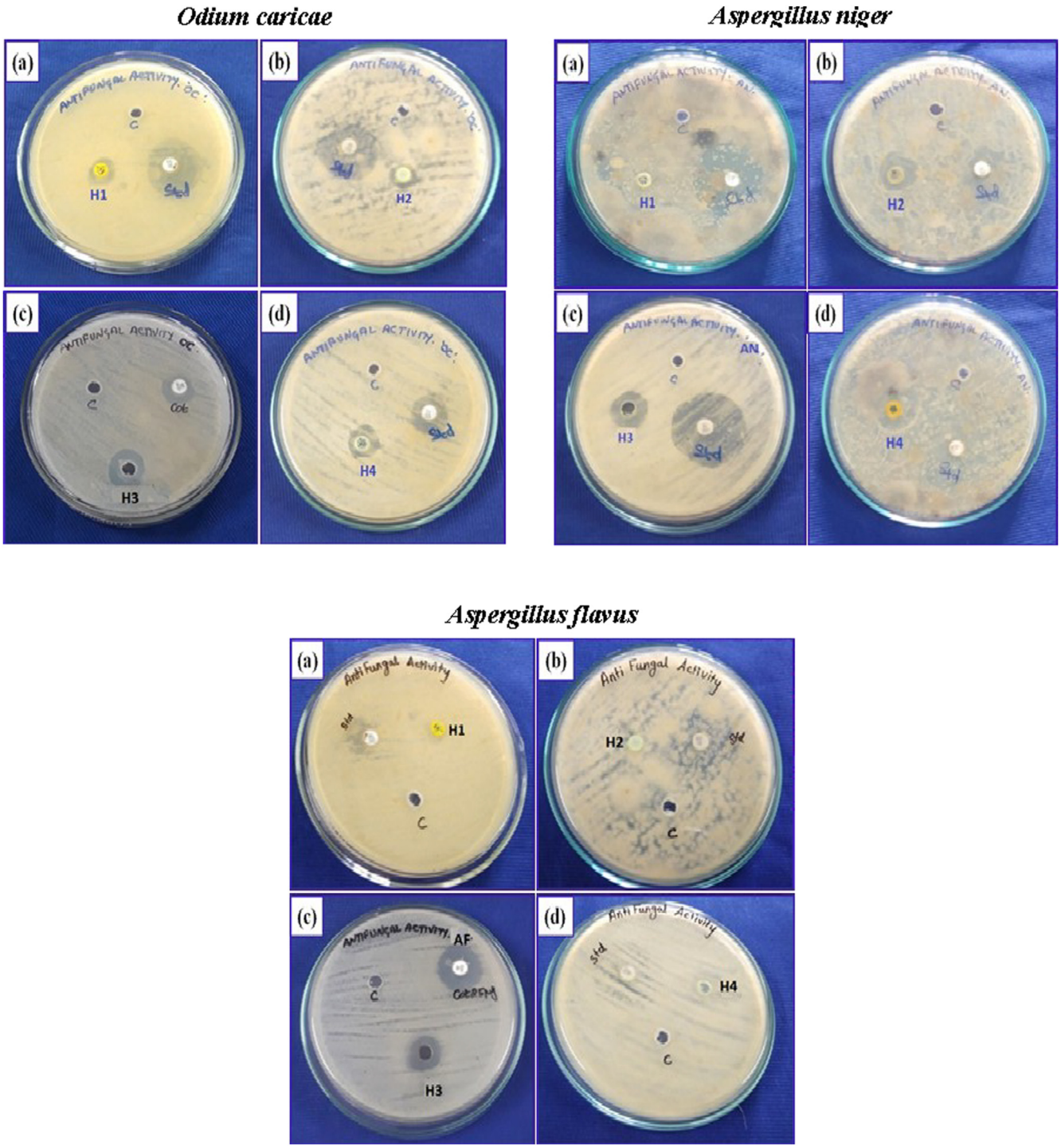

Fig. 11. Antifungal activity of the HAp NPs treated against selected fungi. (a) HAp-Pure, (b) HAp-PEG, (c) HAp-CTAB, and (d) HAp-CE.

The antibacterial activity of HAp without surfactant tested against *S. flexneri* showed a maximum resistance to Amickacin with a 21 mm zone of inhibition. The CE-assisted HAp (H4) NPs exhibited a maximum zone of inhibition of approximately 19 mm against the *S. flexneri* pathogen. HAp NPs synthesized with the surfactants PEG and CTAB (H2, H3) showed significant growth inhibitory effects compared to those of HAp without surfactant (H1). The results confirmed that the green synthesized HAp (curcumin) had good antibacterial activity against the bacterial pathogen *S. flexneri*.

The zones of inhibition for *E. coli* were 9, 11, 23, and 17 mm, whereas for *P. aeruginosa* were 10, 12, 26, and 16 mm, and for *K. pneumonia* were 13, 17, 18, and 14 mm for H1, H2, H3, and H4 samples, respectively. For bacterial pathogens, such as *E. coli*, *P. aeruginosa*, and *K. pneumonia*, HAp with CTAB (H3) showed profound bacterial growth inhibitory effects. The bacterial strain *S. aureus,* a Gram-positive bacterium used for testing the antibacterial activity, showed zones of inhibition of 3, 2, 20, and 4 mm for H1, H2, H3, and H4 samples, respectively. HAp with CTAB (H3) acted as a potent antibacterial agent against the Gram-positive bacterium *S. aureus,* whereas the other three samples, H1, H2, and H4, showed low inhibitory potential. An interesting result was obtained wherein the highest antibacterial activity was identified against *S. aureus* for HAp with CTAB surfactant, which is

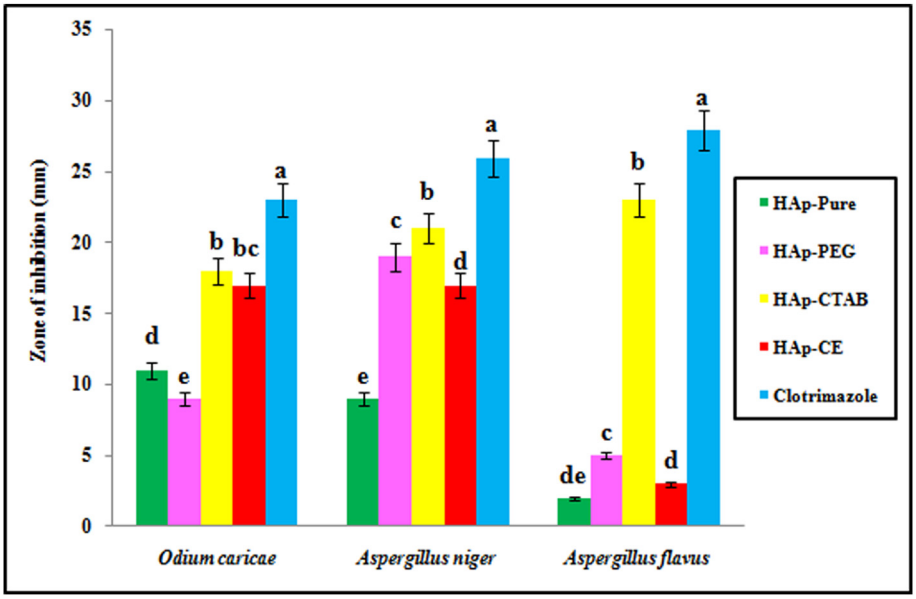

Fig. 12. Antifungal activity of HAp NPs treated against fungal pathogens.

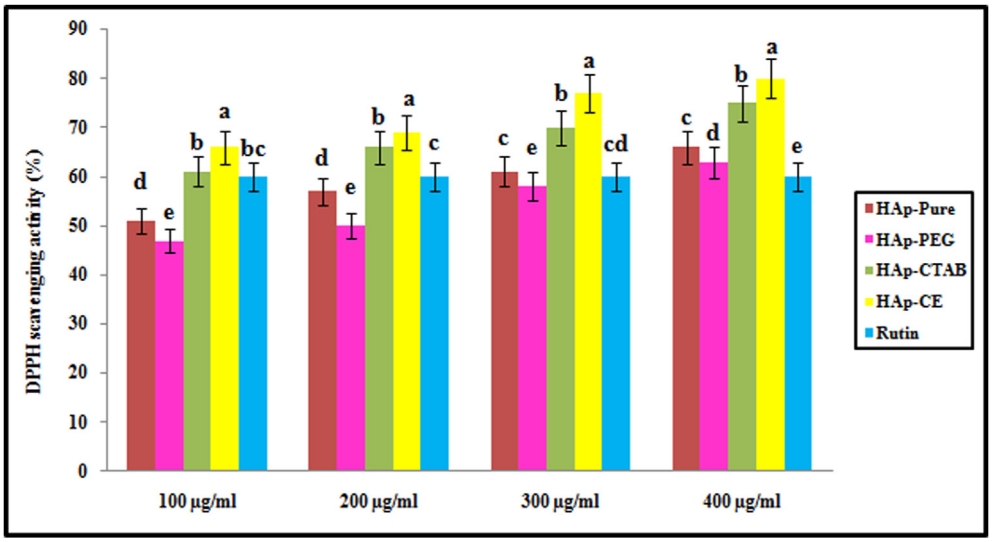

Fig. 13. Antioxidant activity of HAp NPs calcined at 500 °C.

comparable with the standard antibiotic amikacin. HAp NPs exhibited significant antibacterial activity when the particle size was reduced to a nanoscale. Nanosized HAp can interact with the bacterial surface or core where it enters the cell and subsequently exhibits distinct bactericidal mechanisms.

The maximum zone of inhibition was observed in CTAB-assisted HAp NPs against all tested pathogens except *S. flexneri.* The antibacterial activity of HAp NPs depended on the size, morphology, and specific surface area. Smaller particles have stronger bactericidal effects than larger particles due to their larger surface areas for interaction. In the present study, CTAB-assisted HAp showed superior antibacterial activity compared to the other samples as it possesses a smaller crystallite size (24.41 nm). Therefore, stronger zones of inhibition were observed in this study compared to other reported values for HAp. HAp NPs exhibited excellent antibacterial activity, thus, may have greater potential applications in the biomedical field.

3.10. Antifungal activity of HAp nanorods

The antifungal activity of the synthesized HAp NPs was determined via the well diffusion method using sterilized PDA media. The samples were placed in the wells, the plates were incubated at 37 °C for 94 h, and the zones of inhibition were measured in millimeters. Each antifungal assay was performed in triplicate and the mean values were reported.

The antifungal activity of synthesized HAp NPs exhibited zones of inhibition against fungal pathogens, such as *Odium caricae, Aspergillus niger*, and *Aspergillus flavus.* The zones of inhibition exhibited by all fungal strains are shown in Figs. 11 and 12. The sizes of the zones are listed in Supplementary Table 2. The obtained antifungal activity data have been compared to a standard. The standard antibiotic clotrimazole revealed high antifungal activity against all tested species, whereas the four samples (H1, H2, H3, and H4) analyzed for antifungal activity showed moderate and least activity at concentrations of 20, 30, and 40 µg and greater antifungal activity at 50 µg.

The antifungal activity of H1, H2, H3, and H4 samples against *O.*

Fig. 14. Anticancer activity of HAp NPs calcined at 500 °C. (a) HAp-Pure, (b) HAp-PEG, (c) HAp-CTAB, and (d) HAp-CE.

caricae was revealed by the zones of inhibition at 11, 9, 18, and 17 mm, respectively. Among the four samples, HAp with CTAB (H3) showed maximum antifungal activity, whereas HAp with CE had a moderate zone of inhibition. HAp without surfactant (H1) and with PEG (H2) exhibited minimum zones of inhibition. H1, H2, H3, and H4 samples exhibited zones of inhibition of 9, 19, 21, and 17 mm, respectively, for *A. niger*. HAp NPs synthesized with surfactants PEG, CTAB, and CE (H2, H3, and H4) showed significant inhibitory effects compared to HAp without surfactant (H1). A previous study [48] utilizing extract-mediated HAp showed a zone of inhibition of 10 mm against *A. niger*, whereas the present study revealed a much higher zone of inhibition of 17 mm for curcumin-mediated HAp.

The zones of inhibition against *A. flavus* were 2, 5, 23, and 3 mm for H1, H2, H3, and H4, respectively. HAp with CTAB (H3) showed a profound antifungal growth inhibitory effect against the *A. flavus* fungal pathogen. An interesting result was obtained in the present study wherein the highest antifungal activity was identified against *A. flavus* for HAp with CTAB surfactant, compared to the standard antibiotic clotrimazole. From the results, it was observed that the antifungal activity of HAp with CTAB (H3) sample was near to the standard antifungal agent ketokonazole. The antifungal activity suggested that the HAp NPs possessed enhanced antifungal activities.

3.11. Antioxidant activity of HAp nanorods

The human body possesses enzymatic and non-enzymatic antioxidant protections that block the harmful effects of free radicals and other oxidants. Numerous diseases, such as cancer, neural disorders, and cardiovascular diseases, occur due to the creation of free radicals in body tissues. The vital role of antioxidants is the refining of quality of life by inhibiting the formation of free radicals in the body. DPPH assay can predict antioxidant activity by analyzing the scavenging capability of HAp NPs.

Antioxidant properties were analyzed using DPPH, which showed an increase in free radical scavenging activity of HAp NPs. All HAp samples were treated with different concentrations; 100, 200, 300, and 400 µg/ml. The free radical scavenging efficiency of all samples tended to increase with an increase in concentration, as shown in Supplementary Table 3 (Fig. 13).

When standard Rutin exhibited only 60% scavenging activity at all tested concentrations (100-400 µg/ml), the CE-assisted HAp in all concentrations showed the highest scavenging efficiency. Therefore, it was concluded that the HAp NPs with CE possessing effective antioxidant activity can protect the human body against harmful diseases.

3.12. Cytotoxic activity of HAp nanorods against HeLa cell lines

The cytotoxic effects of HAp without surfactant, with surfactants (PEG and CTAB), and CE-assisted HAp were evaluated on the cultured HeLa cell line using an MTT assay, and anticancer images are provided in Fig. 14. HAp NP concentrations influenced the viability of the cells and are presented in Supplementary Table 4. The MTT assay was performed to determine the appropriate dosage by testing various HAp concentrations.

All HAp samples displayed excellent cytotoxicity against HeLa cell lines. The cytotoxic effects of HAp NPs depend on the size of the NPs and the nature of the cell type. Cell viability was identified as 17.24% for the higher concentration 100 µg/ml of HAp without surfactant, and

42.52%, 55.17%, 65.51%, and 90.80%, respectively, for 50, 25, 12.5, and 6.25 μg/ml HAp. A minimum of 100 μg/ml of HAp NPs was sufficient to cause 30% cell mortality.

HAp with the surfactant PEG showed cell viability of 29.78%, 52.68%, 70.96%, 82.79%, and 88.17%, respectively, for 100, 50, 25, 12.5, and 6.25 μg/ml concentrations. HAp with CTAB and CE-assisted HAp showed similar effects on cell viability against HeLa cell lines. The half maximal inhibitory concentration (IC_{50}) was determined as the concentration needed for inhibiting the growth of tumour cells in culture by 50% compared to the untreated cells. From the MTT assay, it was found that all prepared HAp samples (H1, H2, H3, and H4) showed cytotoxic activity against the HeLa cell lines with IC_{50} values of 92.735, 75.114, 97.582, and 77.912 μg/ml, respectively.

HAp NPs hold two different binding sites on the crystal surface; a Ca (Ca^{2+}) site for binding the acidic groups and P (PO_4^{3-}) site for attaching to the basic groups of biomolecules. The negatively charged groups on the surfaces of cancer cells generate more negative charge compared to on normal cells, which are derived from sialic acid residues. HAp NPs showed a high adsorption capacity for sialic acid and could attach to the RBC membrane. HAp NPs are expected to have the highest adhering capacity to cancer cells than normal cells on the basis of electrostatic interactions between the negatively charged sites on the cell membranes and the positively binding sites on the HAp surface. Further HAp NPs penetrate into the cells through endocytosis.

4. Conclusion

The present study concludes that pure HAp, surfactant-assisted HAp, and CE-mediated HAp nanorods are rapidly synthesized. The as-prepared HAp NPs were non-toxic and ecofriendly with an average crystallite size of 40 nm exhibiting rod-like structures, which was confirmed by FE-SEM and TEM micrographs. The XRD analysis revealed that all HAp nanorods possessed hexagonal structures with the space group $P6_3/m$. All the functional groups present in HAp NPs were confirmed by FTIR and Raman analysis, and the observed band assignments indicated that the synthesized samples were high quality HAp nanopowders. No other signals of secondary phases or impurity were detected in the EDAX spectra. HAp NPs exhibited excellent antibacterial activity, thus, greater potential applications in the biomedical field, and were found to possess enhanced antifungal activities. CE-assisted HAp in all concentrations showed the highest scavenging efficiency. Therefore, it is concluded that the HAp NPs with CE possess effective antioxidant activities that can protect the human body against various harmful diseases. All HAp samples displayed excellent cytotoxicity against the HeLa cell lines. The synthesized HAp nanoparticles possessed excellent antibacterial, antifungal, antioxidant, and anticancer activities. The outcomes of this study illustrate that curcumin-encased HAp nanorods play a vital role in the biomedical field.

CRediT authorship contribution statement

Saleth Sebastiammal: Conceptualization, Methodology, Software. **Arul Sigamani Lesly Fathima:** Conceptualization, Supervision, Writing - original draft. **Sandhanasamy Devanesan:** Formal analysis, Writing - review & editing. **Mohamad S. AlSalhi:** Resources, Writing - review & editing, Validation. **Johnson Henry:** Formal analysis. **Marimuthu Govindarajan:** Writing - review & editing. **Baskaralingam Vaseeharan:** Conceptualization, Visualization, Validation.

Declaration of competing interest

None.

Acknowledgements

The authors are grateful to the Deanship of Scientific Research, King Saud University for funding through the Vice Deanship of Scientific Research Chairs. The authors thank the Deanship of Scientific Research and RSSU at King Saud University for their technical support.

Appendix A. Supplementary data

Supplementary data to this article can be found online at https://doi.org/10.1016/j.jddst.2020.101752.

References

[1] S. Sharifi, M. Mokhtarpour, A. Jahangiri, S. Dehghanzadeh, S. Maleki-Dizaj, S. Shahi, Hydroxyapatite nanofibers as beneficial nanomaterial in dental sciences, Biointer. Res. Appl. Chem. 8 (2018) 3695–3699.
[2] S.M. Dizaj, A. Maleki, F. Lotfipour, S. Sharifi, F. Rezaie, M. Samiei, Porous hydroxyapatite-gelatin nanoscaffolds for bone and teeth applications, Biointer. Res. Appl. Chem. 8 (2018) 3670–3673.
[3] S. Ozturk, M. Yetmez, Dynamic analysis of bovine hydroxyapatite/CaTiO3 bioceramics, Biointer. Res. Appl. Chem. 8 (2018) 3232–3236.
[4] R. Subramanian, P. Murugan, G. Chinnadurai, K. Ponmurugan, N.A. Al-Dhabi, Experimental studies on caffeine mediated synthesis of hydroxyapatite nanorods and their characterization, Mater. Res. Express 7 (2020) 015022.
[5] P. Oberbek, T. Bolek, A. Chlanda, S. Hirano, S. Kusnieruk, J. Rogowska-Tylman, G. Nechyporenko, V. Zinchenko, W. Swieszkowski, T. Puzyn, Characterization and influence of hydroxyapatite nanopowders on living cells, Beilstein J. Nanotechnol. 9 (2018) 3079–3094.
[6] A. Rajabnejadkeleshteri, A. Kamyar, M. Khakbiz, Z. Lotfi bakalani, H. Basiri, Synthesis and characterization of Strontium Fluor- Hydroxyapatite nanoparticles for dental applications, Microchem. J. 1 (2020) 153.
[7] M.R. de Rezende, G.F. Andrade, M.F. Cipreste, M.C. Miranda, D.A. Gomes, M.Â. de Barros Correia Menezes, E.M.B. de Sousa, 89Sr-doped hydroxyapatite nanoparticles as a potential therapeutic agent for bone tumors, Int. J. Appl. Ceram. Technol. 16 (2019) 1904–1919.
[8] T.G.P. Galindo, Y. Chai, M. Tagaya, Hydroxyapatite nanoparticle coating on polymer for constructing effective biointeractive interfaces, J. Nanomater. (2019) 2019.
[9] G. Emtiazi, F.A. Shapoorabadi, M. Mirbagheri, Chemical and biological synthesis of hydroxyl apatite: advantage and application, Int. J. Microbiol. Curr. Res. 1 (2019) 20–22.
[10] P. Malmberg, H. Nygren, Methods for the analysis of the composition of bone tissue, with a focus on imaging mass spectrometry (TOF-SIMS), Proteomics 8 (2008) 3755–3762, https://doi.org/10.1002/pmic.200800198.
[11] D.L. Batchelar, M.T.M. Davidson, W. Dabrowski, I.A. Cunningham, Bone composition imaging using coherent-scatter computed tomography: assessing bone health beyond bone mineral density, Med. Phys. 33 (2006) 904–915, https://doi.org/10.1118/1.2179151.
[12] A. Marten, P. Fratzl, O. Paris, P. Zaslansky, On the mineral in collagen of human crown dentine, Biomaterials 31 (2010) 5479–5490, https://doi.org/10.1016/j.biomaterials.2010.03.030.
[13] K.P. Sanosh, M.C. Chu, A. Balakrishnan, T.N. Kim, S.J. Cho, Pressureless sintering of nanocrystalline hydroxyapatite at different temperatures, Met. Mater. Int. 16 (2010) 605–611, https://doi.org/10.1007/s12540-010-0813-1.
[14] M.H. Fathi, A. Hanifi, V. Mortazavi, Preparation and bioactivity evaluation of bonelike hydroxyapatite nanopowders, J. Mater. Process. Technol. 202 (2008) 536–542, https://doi.org/10.1016/j.jmatprotec.2007.10.004.
[15] U. Vijayalakshmi, K. Prabhakaran, S. Rajeswari, Preparation and characterization of sol-gel hydroxyapatite and its electrochemical evaluation for biomedical applications, J. Biomed. Mater. Res. 87 (2008) 739–749, https://doi.org/10.1002/jbm.a.31773.
[16] U. Anjaneyulu, D.K. Pattanayak, U. Vijayalakshmi, Snail shell derived natural hydroxyapatite: effects on NIH-3T3 cells for orthopedic applications, Mater. Manuf. Process. 31 (2016) 206–216, https://doi.org/10.1080/10426914.2015.1070415.
[17] U. Anjaneyulu, D.K. Pattanayak, U. Vijayalakshmi, The facile and phase pure evaluations of nanohydroxyaptite powder by sol-gel method, Int. J. Chem. Tech. Res. 7 (2014) 1516–1520.
[18] U. Vijayalakshmi, S. Rajeswari, Development of silica glass coatings on 316L SS and evaluation of its corrosion resistance behavior in Ringer's solution, Metall. Trans. A. 43 (2012) 4907–4919, https://doi.org/10.1007/s11661-012-1283-5.
[19] C.H. Hou, S.M. Hou, Y.S. Hsueh, J. Lin, H.C. Wu, F.H. Lin, The in vivo performance of biomagnetic hydroxyapatite nanoparticles in cancer hyperthermia therapy, Biomaterials 30 (2009) 3956–3960, https://doi.org/10.1016/j.biomaterials.2009.04.020.
[20] J. Li, Y. Yin, F. Yao, L. Zhang, K. Yao, Effect of nano-and micro-hydroxyapatite/chitosan-gelatin network film on human gastric cancer cells, Mater. Lett. 62 (2008) 3220–3223, https://doi.org/10.1016/j.matlet.2008.02.072.
[21] A. Jungbauer, R. Hahn, K. Deinhofer, P. Luo, Performance and characterization of a nanophased porous hydroxyapatite for protein chromatography, Biotechnol. Bioeng. 87 (2004) 364–375, https://doi.org/10.1002/bit.20121.

[22] K. Purdy, T. Embley, S. Takii, D. Nedwell, Rapid extraction of DNA and rRNA from sediments by a novel hydroxyapatite spin-column method, Appl. Environ. Microbiol. 62 (1996) 3905–3907.
[23] K. Lin, J. Pan, Y. Chen, R. Cheng, X. Xu, Study the adsorption of phenol from aqueous solution on hydroxyapatite nanopowders, J. Hazard Mater. 161 (2009) 231–240, https://doi.org/10.1016/j.jhazmat.2008.03.076.
[24] Y. Hashimoto, T. Taki, T. Sato, Sorption of dissolved lead from shooting range soils using hydroxyapatite amendments synthesized from industrial byproducts as affected by varying pH conditions, J. Environ. Manag. 90 (2009) 1782–1789, https://doi.org/10.1016/j.jenvman.2008.11.004.
[25] M. Sadat-Shojai, Hydroxyapatite: Inorganic Nanoparticles of Bone (Properties, Applications, and Preparation Methodologies), Iranian Students Book Agency (ISBA), Tehran, 2010 (in Persian).
[26] B.A. Fahimmunisha, R. Ishwarya, M.S. AlSalhi, S. Devanesan, M. Govindarajan, B. Vaseeharan, Green fabrication, characterization and antibacterial potential of zinc oxide nanoparticles using *Aloe socotrina* leaf extract: a novel drug delivery approach, J. Drug Deliv. Sci. Technol. (2020) 55.
[27] M.S. AlSalhi, S. Devanesan, P. Shanmugam, Y.O. Kim, J. Kwon, H. Kim, Synthesis and biocompatible role of hierarchical structured carbon nanoplates incorporated α-Fe_2O_3 nanocomposites for biomedical applications with respect to cancer treatment, Saudi J. Biol. Sci. 27 (2) (2020) 588–593.
[28] C. Vijilvani, M.R. Bindhu, F.C. Frincy, M.S. AlSalhi, S. Sabitha, K. Saravanakumar, S. Devanesan, M. Umadevi, M.J. Aljaafreh, M. Atif, Antimicrobial and catalytic activities of biosynthesized gold, silver and palladium nanoparticles from solanum nigurum leaves, J. Photochem. Photobiol. B Biol. 202 (2020).
[29] M.S. AlSalhi, K. Elangovan, A.J.A. Ranjitsingh, P. Murali, S. Devanesan, Synthesis of silver nanoparticles using plant derived 4-N-methyl benzoic acid and evaluation of antimicrobial, antioxidant and antitumor activity, Saudi J. Biol. Sci. 26 (2019) 970–978.
[30] A.A. Alfuraydi, S. Devanesan, M. Al-Ansari, M.S. AlSalhi, A.J. Ranjitsingh, Eco-friendly green synthesis of silver nanoparticles from the sesame oil cake and its potential anticancer and antimicrobial activities, J. Photochem. Photobiol. B Biol. 192 (2019) 83–89.
[31] M. Abinaya, B. Vaseeharan, R. Rekha, S. Shanthini, M. Govindarajan, N.S. Alharbi, S. Kadaikunnan, J.M. Khaled, M.N. Al-Anbr, Microbial exopolymer-capped selenium nanowires – towards new antibacterial, antibiofilm and arbovirus vector larvicides? J. Photochem. Photobiol. B Biol. 192 (2019) 55–67.
[32] M. Divya, B. Vaseeharan, M. Abinaya, S. Vijayakumar, M. Govindarajan, N.S. Alharbi, S. Kadaikunnan, J.M. Khaled, G. Benelli, Biopolymer gelatin-coated zinc oxide nanoparticles showed high antibacterial, antibiofilm and anti-angiogenic activity, J. Photochem. Photobiol. B Biol. 178 (2018) 211–218.
[33] M. Abinaya, B. Vaseeharan, M. Divya, A. Sharmili, M. Govindarajan, N.S. Alharbi, S. Kadaikunnan, J.M. Khaled, G. Benelli, Bacterial exopolysaccharide (EPS)-coated ZnO nanoparticles showed high antibiofilm activity and larvicidal toxicity against malaria and zika virus vectors, J. Trace Elem. Med. Biol. 45 (2018) 93–103.
[34] R. Ishwarya, B. Vaseeharan, S. Kalyani, B. Banumathi, M. Govindarajan, N.S. Alharbi, S. Kadaikunnan, M.N. Al-anbr, J.M. Khaled, G. Benelli, Facile green synthesis of zinc oxide nanoparticles using *Ulva lactuca* seaweed extract and evaluation of their photocatalytic, antibiofilm and insecticidal activity, J. Photochem. Photobiol. B Biol. 178 (2018) 249–258.
[35] A. Iswarya, B. Vaseeharan, M. Anjugam, B. Ashokkumar, M. Govindarajan, N.S. Alharbi, S. Kadaikunnan, J.M. Khaled, G. Benelli, Multipurpose efficacy of ZnO nanoparticles coated by the crustacean immune molecule β-1, 3-glucan binding protein: toxicity on HepG2 liver cancer cells and bacterial pathogens, Colloids Surf. B Biointerfaces 158 (2017) 257–269.
[36] P. Suganya, B. Vaseeharan, S. Vijayakumar, B. Balan, M. Govindarajan, N.S. Alharbi, S. Kadaikunnan, J.M. Khaled, G. Benelli, Biopolymer zein-coated gold nnoparticles: synthesis, antibacterial potential, toxicity and histopathological effects against the zika virus vector *Aedes aegypti*, J. Photochem. Photobiol. B Biol. 173 (2017) 404–411.
[37] V. Karthika, A. Arumugam, K. Gopinath, P. Kaleeswarran, M. Govindarajan, N.S. Alharbi, S. Kadaikunnan, J.M. Khaled, G. Benelli, *Guazuma ulmifolia* bark-synthesized ag, au and Ag/Au alloy nanoparticles: photocatalytic potential, DNA/protein interactions, anticancer activity and toxicity against 14 species of microbial pathogens, J. Photochem. Photobiol. B Biol. 167 (2017) 189–199.
[38] W. Brand-Williams, M.E. Cuvelier, C. Berset, Use of a free radical method to evaluate antioxidant activity, Lebensm.-Wiss. u.-Technol. 28 (1995) 25–30.
[39] K. Azzaoui, A. Lamhamdi, E. Mejdoubi, M. Berrabah, A. Elidrissi, B. Hammouti, S. Zaoui, R. Yahyaoui, Synthesis of nanostructured hydroxyapatite in presence of polyethylene glycol 1000, J. Chem. Pharmaceut. Res. 5 (2013) 1209–1216.
[40] M. Salarian, M. Solati-Hashjin, S. Sara Shafiei, A. Goudarzi, R. Salarian, A. Nemati, Surfactant-assisted synthesis and characterization of hydroxyapatite nanorods under hydrothermal conditions, Mater. Sci. 27 (4) (2009) 961–971.
[41] Y.S. Pan, D.S. Xiong, Influence of dispersant and heat treatment on the morphology of nanocrystalline hydroxyapatite, J. Mater. Eng. Perform. 19 (2010) 1037–1042, https://doi.org/10.1007/s11665-009-9569-5.
[42] L. Kumari, W.Z. Li, S. Kulkarni, K.H. Wu, W. Chen, C. Wang, C.H. Vannoy, R.M. Leblanc, Effect of surfactants on the structure and morphology of magnesium borate hydroxide nanowhiskers synthesized by hydrothermal route, Nanoscale Res. Lett. 5 (2010) 149–157, https://doi.org/10.1007/s11671-009-9457-9.
[43] Y. Liu, D. Hou, G. Wang, A simple wet chemical synthesis and characterization of hydroxyapatite nanrods, Mater. Chem. Phys. 86 (2004) 69–73, https://doi.org/10.1016/j.matchemphys.2004.02.009.
[44] K. Kandori, N. Horigami, A. Yasukawa, T. Ishikawa, Texture and formation mechanism of fibrous calcium hydroxyapatite particles prepared by decomposition of calcium-EDTA chelates, J. Am. Ceram. Soc. 80 (5) (1997) 1157–1164, https://doi.org/10.1111/j.1151-2916.1997.tb02958.x.
[45] A.P. Craig, A.S. Franca, J. Irudayaraj, 7-vibrational spectroscopy for food quality and safety screening, in: A.K. Bhunia, M.S. Kim, C.R. Taitt (Eds.), High Throughput Screening for Food Safety Assessment, Woodhead Publishing, Cambridge, 2015, pp. 165–194.
[46] M. Terauchi, H. Takahashi, N. Handa, T. Murano, M. Koike, T. Kawachi, T. Imazono, M. Koeda, T. Nagano, H. Sasai, Y. Oue, Z. Yonezawa, S. Kuramoto, A new WDS spectrometer for valence electron spectroscopy based on electron microscopy, JEOL (Jpn. Electron Opt. Lab.) News 47 (1) (2012) 23–28.
[47] N.H. Hart, S. Nimphius, R.U. Newton, Mechanical basis of bone strength: influence of bone material, bone structure and muscle action, J. Musculoskelet. Neuronal Interact. 17 (2017) 114–139.
[48] V. Kalaiselvi, R. Mathammal, S. Vijayakumar, B. Vaseeharan, Microwave assisted green synthesis of hydroxyapatite nanorods using *Moringa oleifera* flower extract and its antimicrobial applications, Int. J. Vet. Sci. Med. 6 (2) (2018) 286–295, https://doi.org/10.1016/j.ijvsm.2018.08.003.